Am J Transl Res 2022;14(3):1518-1534
www.ajtr.org /ISSN:1943-8141/AJTR0136224

Original Article

Antibody-conjugated silica-coated gold nanoparticles in targeted therapy of cervical cancer

Hui Yu[1*], Ruxin Zheng[2*], Fei Lei[2*], Wanyue Wang[3], Weikang Guo[2], Lu Zhang[2], Yunduo Liu[2], Xiuwei Chen[2], Yaoxian Wang[2]

Departments of [1]Cardiopulmonary Function, [2]Gynecology, Harbin Medical University Cancer Hospital, Harbin 150081, Heilongjiang, China; [3]School of Basic Medical Science, Qiqihar Medical University, Qiqihar 161006, Heilongjiang, China. [*]Equal contributors.

Received June 10, 2021; Accepted January 18, 2022; Epub March 15, 2022; Published March 30, 2022

Abstract: This study aimed to synthesize silica-coated gold ($Au@SiO_2$) nanoparticles coupled to antibodies against the scavenger receptor class B type I (SR-BI) and investigate their potential ability of visual tracking and treatment of cervical cancer. The fluorescein isothiocyanate (FITC)-labeled $Au@SiO_2$-SR-BI antibody was synthesized, followed by characterization determination. The expression and location of SR-BI protein in cervical cancer cells were respectively detected by western blot and immunofluorescence assays. The effects of nanoparticles on cancer cells were determined by adsorption assay and apoptosis detection, respectively. The effects of nanoparticles on tumor formation in nude mice were determined. The particle sizes of $Au@SiO_2$ ranged from 2-2.5 μm, and the particle size distribution was relatively uniform. MS751 showed the highest expression of SR-BI. SR-BI was located in the cytomembrane. There were more FITC-$Au@SiO_2$-SR-BI nanoparticles on the surface of the cells compared to FITC-$Au@SiO_2$. Significant apoptosis was observed in the FITC-$Au@SiO_2$-SR-BI-treated group in both MS751 and H8 cells. Photothermal ablation of solid tumors was observed when FITC-$Au@SiO_2$-SR-BI was activated using 808 nm wave. Expressions of the apoptosis-related markers including BCL2, BCLX, and p-AKT were significantly decreased, while those of caspase 3 and caspase 8 were significantly increased. The study presented a novel antibody-conjugated $Au@SiO_2$ nanoparticle specifically targeting molecular receptors on cancer cell membranes. Antibody-conjugated $Au@SiO_2$ nanoparticles may have therapeutic potential for the treatment of cervical cancer.

Keywords: $Au@SiO_2$, cervical cancer, gold nanoparticle, antibody, targeted therapy

Introduction

Cervical cancer is the fourth most frequent malignancy in women, with an estimated 528,000 new cases and 266,000 deaths worldwide each year [1]. Nearly 90% of cervical cancer-related deaths occur in developing countries [2]. Early-stage (IA2 to IIA) cervical cancer can be treated with radiotherapy, chemotherapy, or surgery. Unfortunately however, 80% of patients have invasive or metastatic cancer at the time of diagnosis which is nearly always incurable [3, 4]. Thus, there is an urgent need to find new therapeutic modalities to treat this disease.

Recent developments in nanotheranostics offer immense therapeutic and diagnostic potential. Due to the unique physicochemical properties, nanoparticles offer an opportunity to integrate different theranostic modalities into a single nanoplatform for combined real-time diagnosis and treatment of cancers [5-7]. The near-infrared region (800-1200 nm) is the transparency window for human tissues, which is less damaging to the body compared to the other wavelengths of light [8-10]. Nanoparticle-mediated near-infrared photothermal ablation is a novel therapeutic modality in tumors. Upon near infrared laser irradiation, strong near infrared absorption for branched gold nanoparticles induced photothermal-heating to destroy tumor cells. Subsequently, these branched gold nanoparticles were bio-functionalized with cyclo (Arg-Gly-Asp-D-Phe-Glu) targeting peptides cell penetrating-targeting for photothermal cancer treatment applications [11]. Unlike the traditional therapies, such as sur-

gery, radiotherapy, and chemotherapy, nanoparticle therapy is minimally invasive, can be passive or targeted, and has minimal side effects [12, 13]. Gold nanostructures (spherical silica nanoparticles wrapped in nanoscale gold shells), in particular, can not only induce a strong photothermal response under near-infrared excitation, but they are also attractive probes for cancer cell imaging due to their tunable localized surface plasmon resonance [6, 14, 15]. Therefore, gold nanostructures are being studied as a promising platform for cancer therapy and diagnosis, and have presented 100% efficacy in the remission of tumors [16, 17].

At present, the synthesis of gold nanoparticles in the near-infrared region is complicated and needs large amounts of organic solvents. Silica (SiO_2) is widely applied in biomedicine due to its high stability, minimal immunogenicity, and good biocompatibility, all of which provide favorable conditions for the coating of other materials [18]. Gold nanoparticles on the modified SiO_2 particles are used as seed crystal and nucleation points, and the prepared silica-coated gold nanoparticles (Au@SiO_2) can highly regulate the linear optical absorption properties [19]. Au@SiO_2 nanoparticles have therefore become one of the most promising systems for photothermal treatment [20].

Herein, we report our efforts to develop an amino-modified Au@SiO_2 coupled with antibodies to a cervical cancer-specific protein (scavenger receptor class B type I [SR-BI]) as a novel theranostic platform and investigate its potential ability of visual tracking and treatment of cervical cancer.

Experimental details

Synthesis of Au@SiO_2

For the synthesis of gold nanoparticles, chloroauric acid ($HAuCl_4$) was used as a metal precursor, ascorbic acid as a reducing agent, and polyvinylpyrrolidone (PVP) as a capping material. Briefly, 300 mM of ascorbic acid and a certain amount of PVP were added to 100 mM aqueous solution of $HAuCl_4$, followed by ultrasonic treatment for 10 min. After centrifugation and three washes, the product was freeze dried. Then 0 mM (A), 5 mM (B), 15 mM (C), and 25 mM (D) prepared gold nanoparticles were added to three-mouth flasks respectively, and 15 mL pure water and 30 mL isopropanol were added to each of them followed by ultrasonic dispersion for 10 min. After the ultrasonic treatment, 15 mL ammonia was slowly added to each of them, followed by 20 mM 3-aminopropyltriethoxysilane (APTES) and incubated with mechanical stirring for 12 h at room temperature (25°C). The products were washed with deionized water until a pH of 7 was obtained, and then washed with anhydrous ethanol more than five times. Finally, the products were vacuum freeze-dried for 10 h, and the dried products were collected and stored in the absence of air. All the reagents used were purchased from Aladdin Biochemical Technology Co. Ltd., Shanghai, China.

Preparation of fluorescein isothiocyanate (FITC)-labeled Au@SiO_2

$NaHCO_3$ (30.2 mg), Na_2CO_3 (4.2 mg), and NaCl (29.4 mg) were weighed precisely and placed in a clean round-bottom flask, and 4 mL ultrapure water was added to dissolve them. Then, 5 mg of FITC and 3 mM of APTES were added to the flask and stirred at 4°C for 8 h. The solution was then transferred to a dialysis bag (500 MWCO) and was placed in a 1 L beaker for dialysis at 4°C for 24 h. The water was changed every hour for the first two hours, then every two hours, and finally it was changed every five to six hours to obtain Product A. Product A was evenly mixed with 3 mM APTES and then according to the steps of preparing Au@SiO_2, the FITC-labeled Au@SiO_2 was prepared. All the preparatory procedures were carried out in the dark. All the reagents used were purchased from Aladdin Biochemical Technology Co. Ltd., Shanghai, China.

Preparation of FITC-Au@SiO_2-SR-BI antibody

A total of 100 mg of FITC-Au@SiO_2 was dispersed in 5 mL of PBS solution and treated with ultrasonic dispersion. Then, 600 μL of SR-BI antibody (ab217318; Abcam, Cambridge, MA, USA) was added and stirred, followed by the addition of 20 mg genipin (Maclean Biochemical Technology Co. Ltd., Shanghai, China) and stirred at room temperature for 2 h followed by constant stirring for 12 h at 2-8°C. After centrifugation at 10,000 rpm for 5 min, the products were collected and freeze-dried. The preparatory procedures were carried out in the

dark. The schematic illustration is shown in Figure S1.

Characterization of nanoparticles

The Au@SiO_2 particles were characterized using dynamic light scattering (DLS), morphological observations, X-ray diffraction (XRD) detection, and Au element content analysis. Briefly, a certain amount of the prepared products was added to 2 mL ultra-pure water, and then placed into the sample pool following ultrasonic treatment. The particle size and distribution of potential of the samples were quickly tested on a Zetasizer Nano S90 (Malvern Instruments Ltd., Malvern, UK). For morphological observations, the prepared products were placed on the sample table with a conductive adhesive, sprayed with gold under argon atmosphere, and observed using a Hitachi-S4800 scanning electron microscope (SEM) (HITACHI, Tokyo, Japan). For XRD detection, the prepared products were ground and filled on the sample plate. The scanning range was set as 4-60°, and the samples were analyzed on the D8 Advance with DaVinci X-ray diffractometer (Bruker, Germany). The Au element content was determined through SEM.

The fluorescence characteristics of FITC-Au@SiO_2 were determined. Briefly, the prepared products were dispersed in water, and dropped on a glass slide. The fluorescence was observed under FITC channel under a fluorescence microscope (BX53; Olympus, Japan).

The infrared characteristics of FITC-Au@SiO_2-SR-BI were detected using infrared spectroscopy. Briefly, the prepared products were mixed with specpure potassium bromide and ground. The infrared characteristics were tested after tableting using a Nicolet 6700 FT-IR spectrometer (Thermo Scientific, USA).

Cell culture

Human cervical epithelial (H8) and cervical cancer-derived (Ca Ski) cell lines were cultured in 90% RPMI1640 medium (Gibco, Grand Island, NY) supplemented with 10% fetal bovine serum (FBS) and 1% penicillin/streptomycin (P/S); human endometrial adenocarcinoma (HEC-1-A) cells were cultured in 90% McCoy's 5A (Gibco) medium containing 10% FBS and 1% P/S; human cervical epidermoid carcinoma (MS751) and human cervical carcinoma (C-33 A) cells were maintained in 90% Eagle's minimum essential medium (MEM) supplemented with 10% FBS and 1% P/S; Hela cells were cultured in 90% MEM with 10% FBS, 1% sodium pyruvate, and 1% P/S. All cells were cultured at 37°C in a 5% CO_2 atmosphere.

Western blotting

The cells were lysed in RIPA lysis buffer (Beyotime, China) with phenylmethylsulfonyl fluoride (PMSF, Beyotime) for protein extraction. Concentrations of all the protein samples were determined with a BCA Protein Assay Kit (Thermo Scientific, Rockford, IL, USA). The proteins were separated using 10% sodium dodecyl sulfate polyacrylamide gel electrophoresis (SDS-PAGE) and transferred onto polyvinylidene fluoride (PVDF) membrane (Millipore, Billerica, MA, USA), followed by blocking with 5% non-fat milk for 1-2 h at 37°C. Then the membrane was incubated with rabbit anti-SR-BI (1:2000; Abcam) and mouse anti-β-actin (1:1000; Abcam) monoclonal antibodies at 4°C overnight. Following that the membrane was incubated with an anti-rabbit IgG-HRP antibody (1:5000) at 37°C for 2 h. Specific protein bands were photographed, and quantification of the reactive proteins was performed using an ECL chemiluminescence system (Santa Cruz). Blots were detected by ECL system (Millipore) and analyzed using Tanon Image Software (Tanon, Shanghai, China).

Immunofluorescence assay

H8 and MS751 cells growing in logarithmic phase were used in this experiment. Briefly, 2×10^5 H8 cells and 3×10^5 MS751 cells were plated in 24-well plates at 0.5 mL/well. The cells were fixed in 4% paraformaldehyde for 15 min, and washed thrice for 3 min. Then the cells were permeabilized with 0.5% Triton X-100 for 20 min at room temperature. After washing thrice with PBS for 3 min, the cells were blocked with 10% goat serum for 1 h at room temperature. Then, the cells were incubated with the primary antibody (rabbit anti-SR-BI monoclonal antibody; 1:100) in 10% goat serum at 4°C overnight, followed by incubation with goat anti-rabbit IgG (H+L) cross-adsorbed secondary antibody conjugated to Alexa Fluor 555 (1:200; Thermofisher, USA). Then the cells were mounted with anti-fluorescence quenching mounting

solution (P0131, Beyotime). Finally, the cells were visualized using a fluorescence microscope (Olympus, IX73, Japan).

Laser confocal scanning microscopy

H8 and MS751 cells growing in logarithmic phase were used. The prepared nanoparticles were dissolved and added to the media of the following four groups: control, Au@SiO_2, FITC-Au@SiO_2, and FITC-Au@SiO_2-SR-BI. The amount of nanoparticle added to the cell culture medium was based on the gold element content (each milliliter medium contained 1.5 mg of gold element). After incubation with the nanoparticles for 24 h, the cell intake and uptake sites were observed under a laser confocal scanning microscope (Leica, SD AF, Germany), and detected based on the FITC marker.

TUNEL assay

The nanoparticles were added to H8 and MS751 cell culture media as described above. Twenty-four hours after the addition of the nanoparticles, the cells were irradiated with far-infrared light at 808 nm with an energy density of 2 W/cm^2. The infrared irradiation methods referred to previous studies [8, 21-23] as well as our preliminary experiments. After 5 min of treatment, the medium was replaced with fresh one without the nanomaterials, and cell apoptosis was analyzed after 24 h using the in-situ terminal deoxynucleotidyl transferase dUTP nick end labelling (TUNEL) assay. Briefly, cells were fixed in 4% paraformaldehyde for 30 min, permeabilized in 0.3% Triton X-100 for 5 min at room temperature and treated with 50 μL TUNEL reagent for 60 min in 37°C in the dark. After being mounted with anti-fluorescence quenching mounting solution (P0131, Beyotime), the cells were visualized using a fluorescence microscope (Olympus, IX73, Japan). The excitation and emission wavelengths of Cy3 were 550 and 570 nm (red fluorescence), respectively.

Tumor-bearing animal model

Female Balb/c nude mice (4 weeks old) weighing 18±2 g were purchased from JiHui experimental animal breeding company (Shanghai, China). All animals received human care in compliance with the guidelines of The Second Affiliated Hospital of Harbin Medical University for the maintenance and use of laboratory animals in research. All the experimental protocols involving live animals were reviewed and approved by the Animal Experimentation Committee of The Second Affiliated Hospital of Harbin Medical University. MS751 cervical cancer cells were trypsinized from the tissue culture flasks. Prior to the injection, the cells were counted and suspended in sterile phosphate buffer saline (PBS) at a density of 5×10^7/mL. To induce tumor growth, a 100 μL volume of the cell suspension was injected in the armpit of the right forelimb of three mice in the pre-experimental studies, which served as tumor donors for the subsequent experiments. Tumor growth was monitored after two weeks, and the tumor volume was calculated. The tumors in the pre-experimental mice were cut into 1 mm^3 pieces and inserted into the armpits of 47 nude mice. When the tumors grew to 100 mm^3, 24 nude mice with uniform tumor size were selected and randomly divided into four groups with six mice per group. The mice in group E were injected with saline solution in the tail vein, mice in group F were injected with FITC-Au@SiO_2, and those in group G were injected with FITC-Au@SiO_2-SR-BI. The mice in groups E, F, and G were all irradiated with infrared ray. Briefly, the mice were anesthetized with 5% chloral hydrate at a dose of 0.08 mL/10 g. After the mice were anesthetized, their limbs and teeth were bound with ropes. After the mice were fixed, local infrared irradiation was performed. The wavelength of infrared irradiation was 808 nm, the intensity was 2 W/cm^2, and the irradiation time was 5 minutes. The mice in group H were injected with FITC-Au@SiO_2-SR-BI without any infrared irradiation. The volume of nanoparticle solution injected into the mice was 100 μL, which had a gold concentration about 1.5 mg of Au/mL.

The temperature of the mice in groups E, F, and G was measured 1, 3, and 5 min after irradiation with the infrared rays. The body weight and tumor volume of the mice in groups E, F, G, and H were measured on days 1, 4, 7, 10, and 13 during the experiment. At the end of 15 days, the mice were sacrificed and their tumors were collected and stored at -80°C until further investigation. Tumor tissues from the mice in each of the four groups were analyzed by hematoxylin and eosin (HE) staining. TUNEL assay

Table 1. The primer sequences of the detected genes

Primer	Sequence (5'-3')
BCL2-hF	GACTTCGCCGAGATGTCCAG
BCL2-hR	GGTGCCGGTTCAGGTACTCA
BCLX-hF	GTGCGTGGAAAGCGTAGACA
BCLX-hR	TCTCGGCTGCTGCATTGTT
mTOR-hF	CCTTATGGTGCGGTCCCTT
mTOR-hR	AGCCAGCCTGCCACTCTTG
caspase 8-hF	TGCCCAAACTTCACAGCATTA
caspase 8-hR	TTCAAAGGTCGTGGTCAAAGC
GAPDH-hF	TGACAACTTTGGTATCGTGGAAGG
GAPDH-hR	AGGCAGGGATGATGTTCTGGAGAG

was performed on the tumor tissue samples to analyze the apoptotic rate of the cells.

The expression of apoptosis-related genes including B cell lymphoma 2 (BCL2), B cell leukemia X (BCLX), mammalian target of rapamycin (mTOR), and caspase 8 in the mice tumor tissues were analyzed using quantitative polymerase chain reaction (qPCR). After lysis of the tumor tissues with TRIzol (9109, TAKARA), RNA was extracted with chloroform. The PCR reaction volume was 20 μL, which included 4 μL of primer and 1 μL total RNA. The sequences of the primers used are shown in **Table 1**. The cDNA obtained was amplified by fluorescence quantitative PCR instrument (7900HT FAST, ABI). Furthermore, the expressions of caspase-3, BCL-2, glyceraldehyde-3-phosphate dehydrogenase (GAPDH), and phospho-protein kinase B (p-AKT) in the mice tumor tissues were analyzed using western blotting.

Statistical analysis

Results are expressed as mean ± standard deviation (SD). All data were analyzed using Graphpad prism 5.0 software (GraphPad Prism, San Diego, CA). Differences for three or more groups were analyzed using one-way ANOVA. *P* value <0.05 was considered to be statistically significant.

Results and discussion

Characterization of Au@SiO_2

The results of particle size analysis showed that the particle sizes of nanoparticles prepared with different raw material ratios were different (**Figure 1A**). The particle size distribution range was narrow for groups A, B, and C, which met the requirements. There were two kinds of particle sizes in group D. The hydration particle size of the blank group (A) was larger, while there was little difference between groups B and C (2-2.5 μm).

According to the potential analysis diagram of the nanoparticles, the particles prepared with different raw material ratios all had negative potential, but the potential values were different (**Figure 1B**). The main raw material of the nanoparticles surface was SiO_2, therefore all the nanoparticles had negative potential. The different potential values were caused by the different content of SiO_2 on the surface. Additionally, the absolute values of potential were all more than 0, indicating that particles could stably exist in aqueous solution.

The SEM of the particles showed that the shapes of the particles prepared with different material ratios were all round or quasi-round, and the particle size distribution was relatively uniform (**Figure 1C**).

As shown in **Figure 1D**, a peak shape appeared at 2θ=29°, which was the characteristic peak of amorphous SiO_2. The peaks at 2θ=38° and 44° were the characteristic diffraction peaks of Au. The spectra showed that the materials contained SiO_2 and Au.

In terms of elemental analysis, Au element was found in groups B, C, and D. Group C had the most Au content, followed by group B, while group D had the least Au content. Thus, group C was considered suitable for our experimental requirements (**Figure 1E**).

Characterization of FITC-Au@SiO_2 and FITC-Au@SiO_2-SR-BI

As shown in **Figure 2A**, irregular agglomeration of FITC-Au@SiO_2 particles occurred in dry state, which could be seen under a fluorescence microscope. The nanoparticles emitted green fluorescence under the excitation of incident light, indicating that the nanoparticles were successfully coupled with FITC.

As shown in **Figure 2B**, the absorption peaks around 1200 cm^{-1}, 815 cm^{-1}, and 478 cm^{-1} were the bending vibration of Si-O-Si, while that

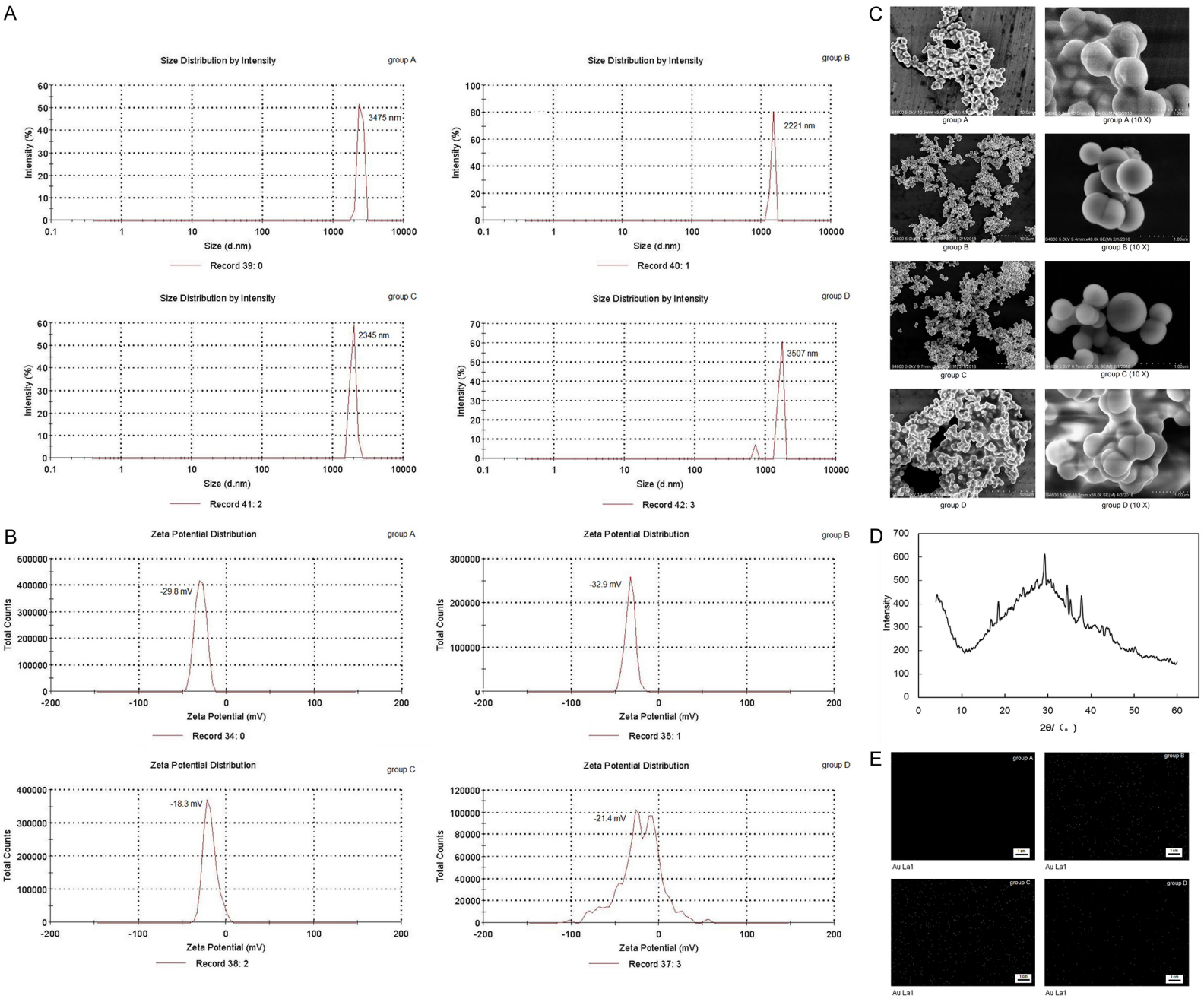
A
Size Distribution by Intensity
group A
3475 nm
Intensity (%)
Size (d.nm)
Record 39: 0
Size Distribution by Intensity
group B
2221 nm
Intensity (%)
Size (d.nm)
Record 40: 1
Size Distribution by Intensity
group C
2345 nm
Intensity (%)
Size (d.nm)
Record 41: 2
Size Distribution by Intensity
group D
3507 nm
Intensity (%)
Size (d.nm)
Record 42: 3
B
Zeta Potential Distribution
group A
-29.8 mV
Total Counts
Zeta Potential (mV)
Record 34: 0
Zeta Potential Distribution
group B
-32.9 mV
Total Counts
Zeta Potential (mV)
Record 35: 1
Zeta Potential Distribution
group C
-18.3 mV
Total Counts
Zeta Potential (mV)
Record 38: 2
Zeta Potential Distribution
group D
-21.4 mV
Total Counts
Zeta Potential (mV)
Record 37: 3
C
group A
group A (10 X)
group B
group B (10 X)
group C
group C (10 X)
group D
group D (10 X)
D
Intensity
2θ/ (°)
E
group A
Au La1
group B
Au La1
group C
Au La1
group D
Au La1

Figure 1. Particle size analysis diagrams (A), potential analysis diagrams (B), and scanning electron microscope diagrams (C) of Au@SiO_2 prepared using different raw material ratios (group A-D). X-ray diffraction patterns of Au@SiO_2 (D). Energy spectra of Au@SiO_2 prepared using different material ratios (group A-D) detected by scanning electron microscopy (E). Photo magnification, 5,000×, 3,000× (left) or 30,000×, 40,000×, 50,000× (right) for (C), and 10× for (E).

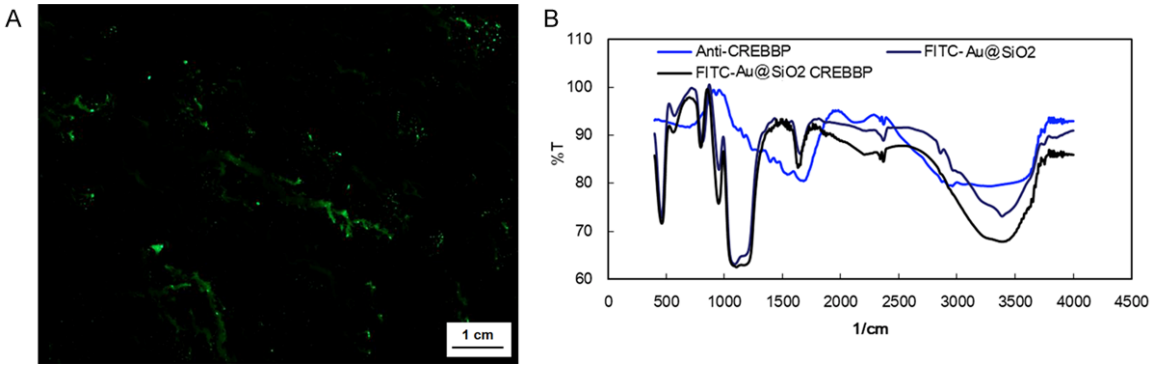

Figure 2. Scanning electron microscopy images of fluorescein isothiocyanate (FITC)-labeled Au@SiO_2 (A). Infrared spectrum of FITC-labeled Au@SiO_2-SR-BI (B). Photo magnification, 10×.

around 962 cm^{-1} was the bending vibration of Si-OH, which proved the existence of SiO_2. The wide peak between 3300 and 3500 was the characteristic absorption peak of amino, suggesting that the antibody was successfully coupled on the surface of the nanoparticles.

Expression and location of SR-BI in cervical cancer cells

The expression levels of SR-BI in the five cervical cancer cell lines (HEC-1-A, MS751, Caski, C-33A and Hela) and normal cervical epithelial cells (H8) were detected by western blotting. As shown in **Figure 3A**, SR-BI had the highest expression level in MS751 cells. Moreover, we repeated the western blotting for H8, MS751, and Hela again, and MS751 cells showed the highest expression level of SR-BI (**Figure 3B**). Therefore, MS751 and H8 cell lines were used in the subsequent experiments. Immunofluorescence analysis of SR-BI showed that SR-BI was located on the cytomembrane (**Figure 3C**).

Adsorption of nanoparticles

The adsorption of nanoparticles on cells was observed using a laser confocal scanning microscopy. As shown in **Figure 4**, compared with FITC-Au@SiO_2, there were more FITC-Au@SiO_2-SR-BI nanoparticles on the surface of cells. Additionally, there was no significant difference in the adsorption between MS751 and H8 cells.

Apoptosis assay

There was almost no apoptosis without infrared irradiation in both nanoparticle groups with and without coupled antibodies. Additionally, there were also fewer apoptotic cells following infrared irradiation in the nanoparticle group without coupled antibody (FITC-Au@SiO_2), suggesting that the nanoparticles were rarely absorbed by cells without antibody. Furthermore, significant apoptosis was identified in FITC-Au@SiO_2-SR-BI group in both MS751 and H8 cells, without significant difference between the two types of cells (**Figure 5**).

Tumor formation in nude mice

There was no significant difference in the body weight of the mice among the four groups (**Figure 6A**), which indicated that infrared exposure did not affect the weight of the mice. Additionally, there was no significant difference in tumor volume among the groups E, F, and H. On the 7, 10, and 13 day of the experiment, the tumor volume in group G decreased significantly compared with that in the other groups ($P<0.0001$) (**Figure 6B**). The results indicated that the antibody-conjugated nanoparticles had stronger targeting properties. Following infrared irradiation, the tumor volume was

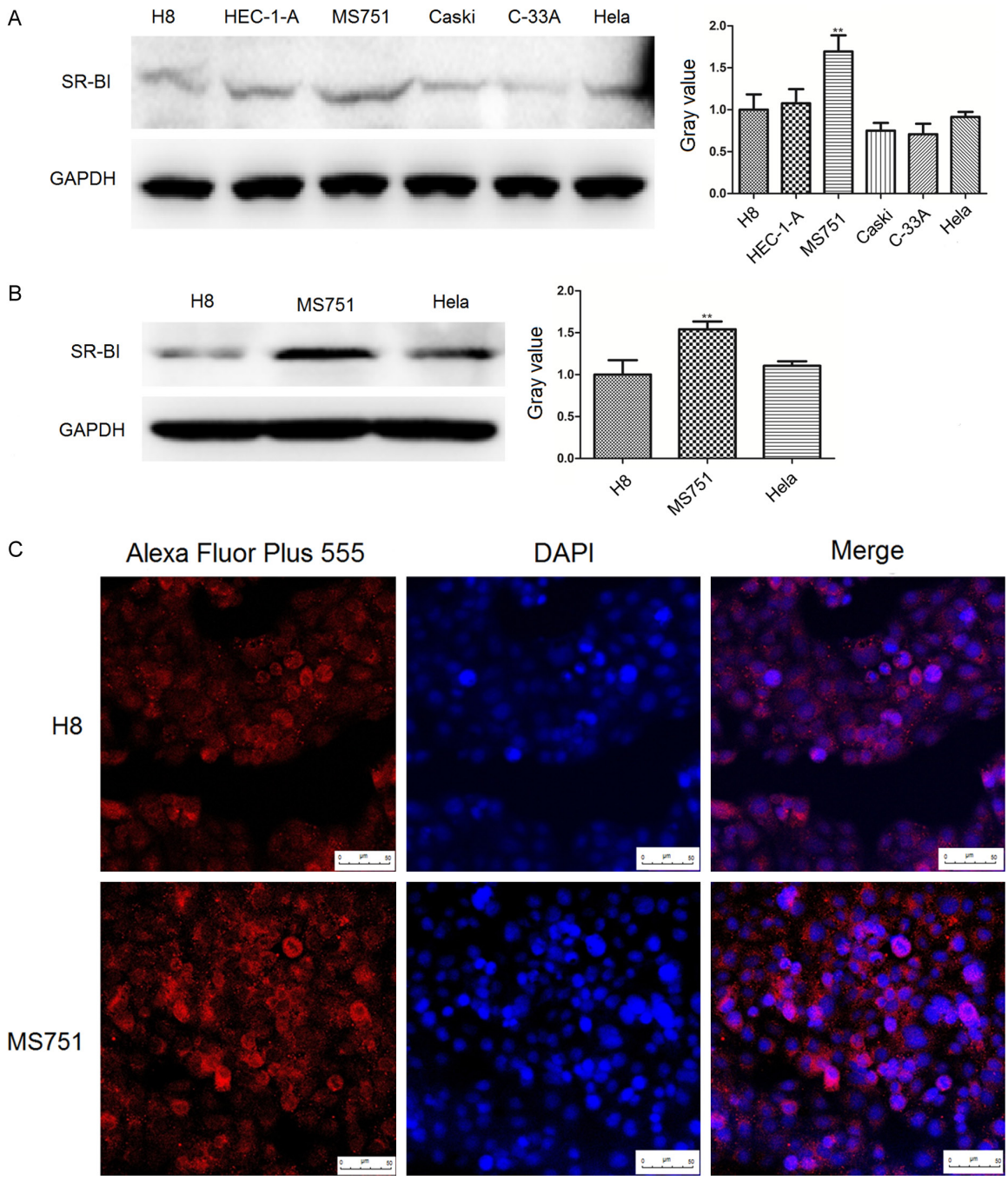

Figure 3. Expression level (A and B), and location (C) of SR-BI in cervical cancer cells detected using western blotting and immunofluorescence analysis, respectively. ***P<0.001 compared with H8. SR-BI expression is highest in MS751 cells. SR-BI is localized in the cell membrane. Photo magnification, 200×.

markedly reduced, showing therapeutic potential (**Figure 6D**). For the tumor surface temperature, compared with group E, the tumor surface temperature of group F and group G increased significantly after 1 and 3 min of irradiation. Compared to group F, the tumor surface temperature of group G increased significantly after 1 and 3 min of irradiation (P<0.0001) (**Figure 6C**).

The results of the HE staining showed no significant abnormalities in cells in groups E, F, and H (**Figure 7A**). While most cells in group G showed contraction, partial cell lysis, and necrosis. The

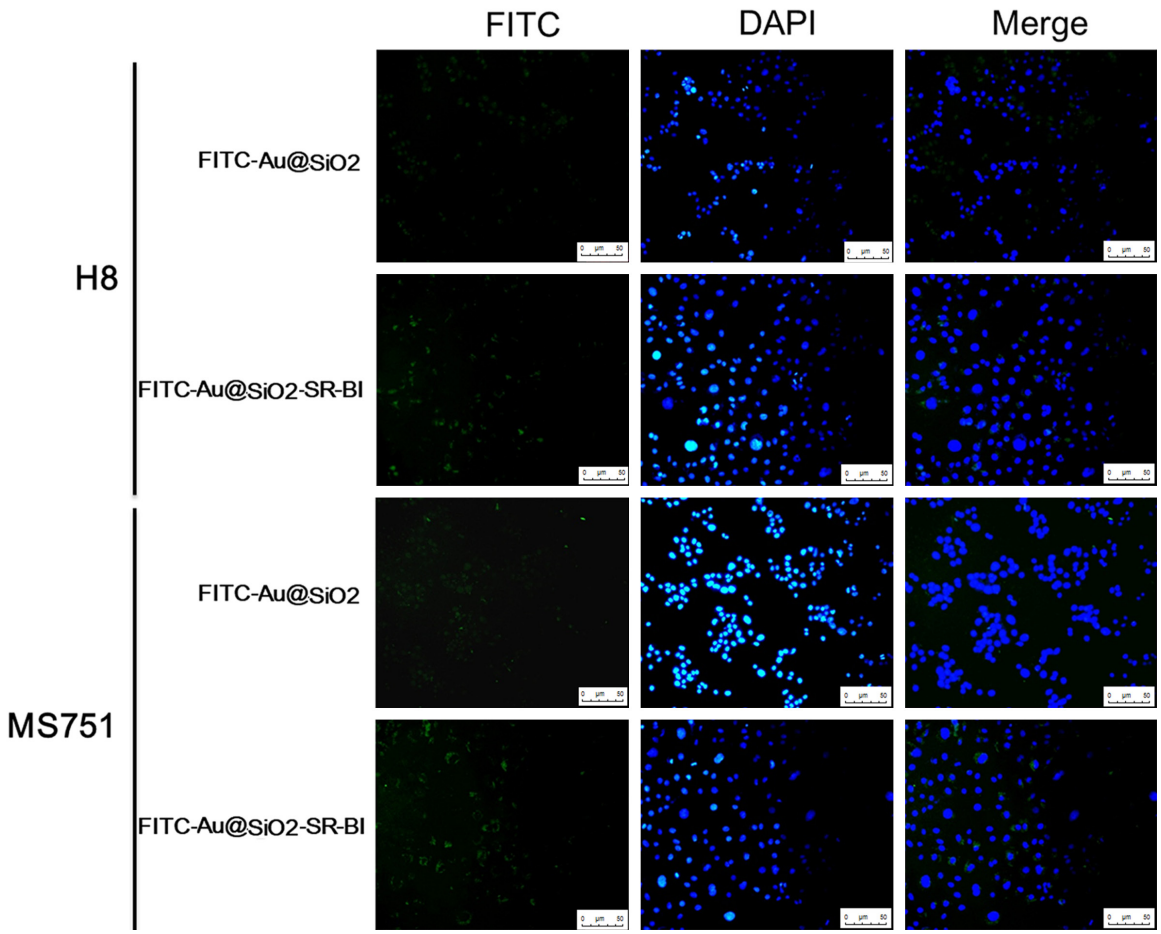

Figure 4. Adsorption of nanoparticles on cells observed using a laser confocal scanning microscopy. More FITC-Au@SiO_2-SR-BI nanoparticles were observed on the surface of cells compared to FITC-Au@SiO_2. Photo magnification, 200×.

results of the TUNEL staining revealed that compared to group E, there was no significant difference for the apoptotic rate in groups F and H, while the apoptotic rate was significantly increased in group G (**Figure 7B**). The q-PCR results of the tissue samples are shown in **Figure 8A**. Compared to group E, the expression of BCL-2, BCLX, and mTOR were significantly decreased in group G, while the expression of caspase 8 was significantly increased in group G. Compared to group G, the expression of BCL-2 and BCLX in group H increased significantly, while the expression of caspase 8 decreased significantly.

Western blot analysis of tissues showed that compared to group E, p-AKT and BCL2 were significantly decreased in groups F, G, and H, while caspase 3 was significantly increased in groups F, G, and H. Compared to group G, p-AKT and BCL2 were significantly increased in group H, while caspase 3 was significantly decreased in group H (**Figure 8B**). Most patients with cervical cancer receive standard radiotherapy and chemotherapy, however, the clinical outcomes vary significantly [24]. Therefore, there is a crucial need for therapeutic advances. Hyperthermia, which is based on the direct application of heat to destroy the solid tumor, is an attractive therapeutic approach for cancer treatment. Exogenous tumor-targeted heating nanophase materials, such as Au@SiO_2, have been developed to provide specific heating of the tumor regions while minimize thermal damage to normal tissues. It has been reported that nanoparticle-mediated photothermal ablation is effective in various human cancers, including colon [25], brain [26], breast [27], and prostate cancer [28-31]. In this study, Au@SiO_2 was synthesized and characterized for

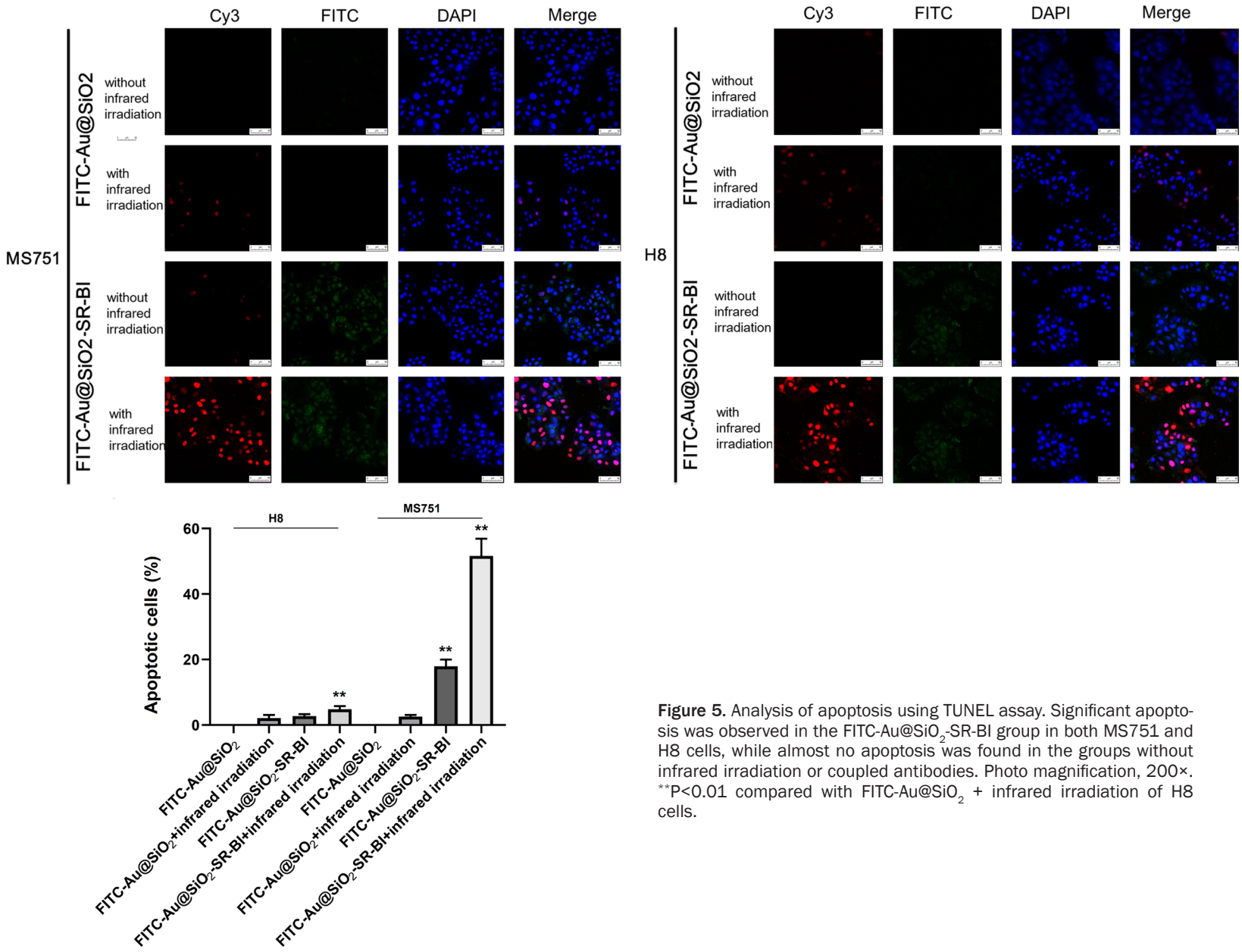

Figure 5. Analysis of apoptosis using TUNEL assay. Significant apoptosis was observed in the FITC-Au@SiO$_2$-SR-BI group in both MS751 and H8 cells, while almost no apoptosis was found in the groups without infrared irradiation or coupled antibodies. Photo magnification, 200×. **P<0.01 compared with FITC-Au@SiO$_2$ + infrared irradiation of H8 cells.

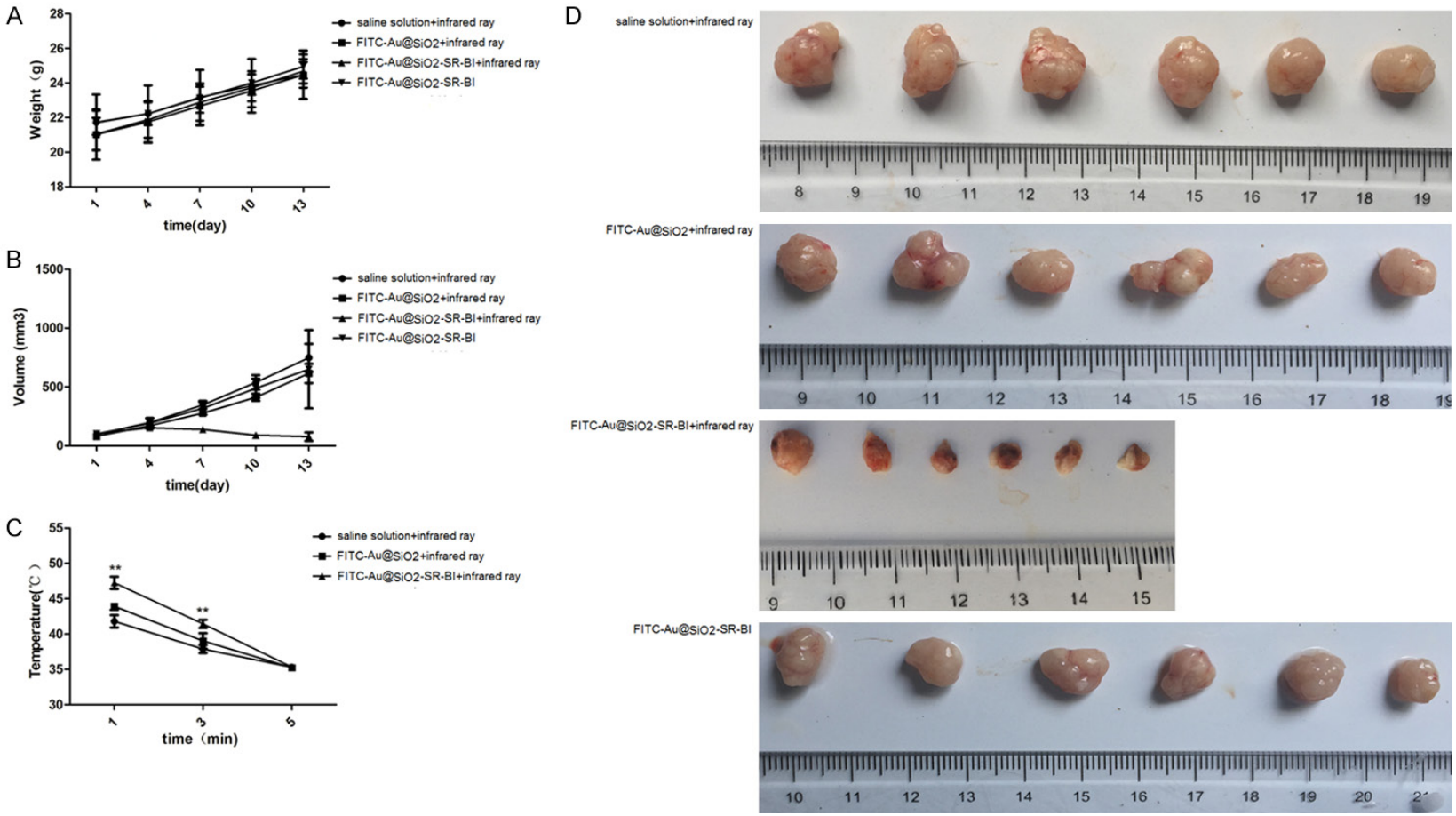

Figure 6. Effect of nanoparticles on tumor formation in nude mice. Monitoring of animal weights (A). Monitoring of tumor volumes (B). Tumor surface temperatures in the infrared irradiation groups (C). Pictures of animal tumors after differential processing (groups E-H) (D). **P<0.01 compared with saline solution + infrared ray.

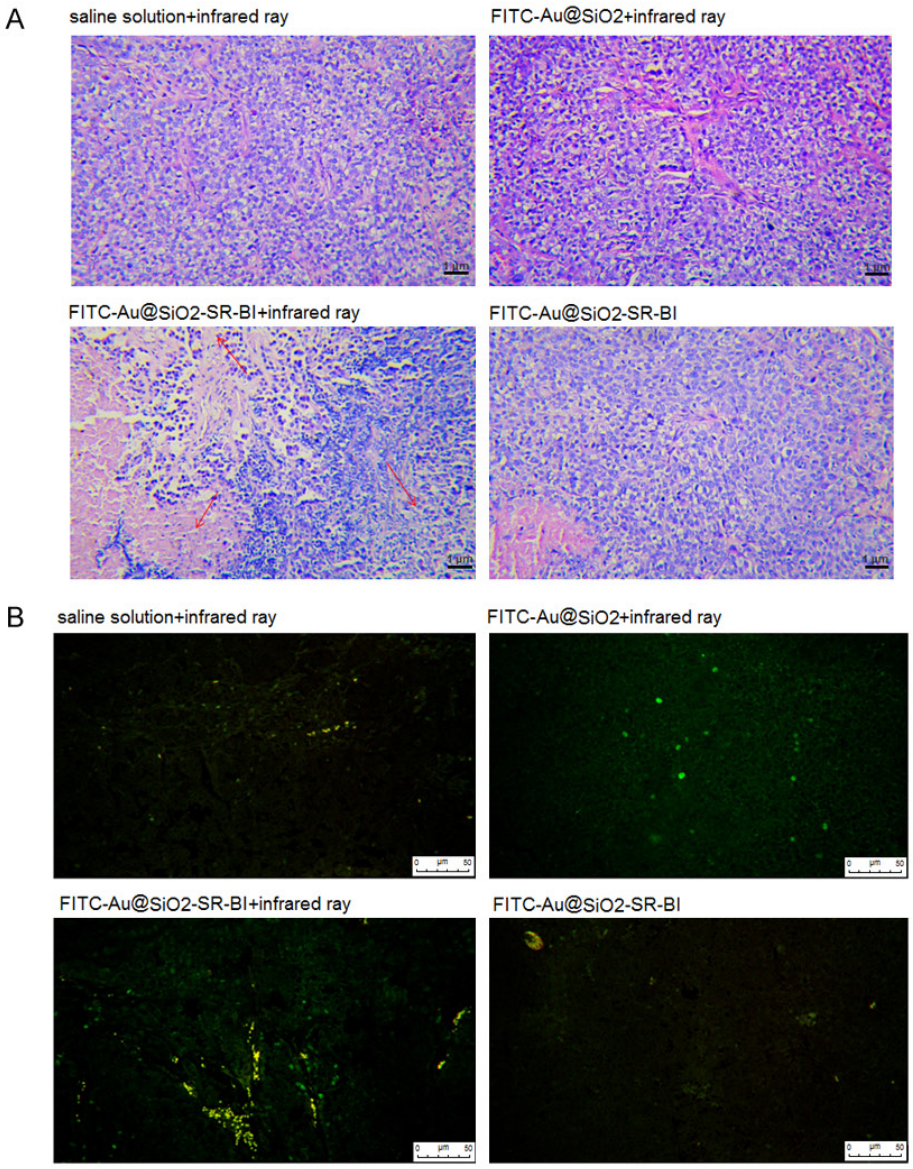

Figure 7. Histological images of hematoxylin and eosin staining after differential processing (groups E-H) (A). The area indicated by the black arrow is an obvious lesion. Photo magnification, 200×. TUNEL staining after differential processing (groups E-H) (B). The yellow-green dots represent apoptotic cells. Photo magnification, 200×. $^{**}P<0.01$ compared with saline solution + infrared ray, $^{\#\#}P<0.01$ compared with FITC-Au@SiO_2 + infrared ray, $^{\&\&}P<0.01$ compared with FITC-Au@SiO_2-SR-BI + infrared ray.

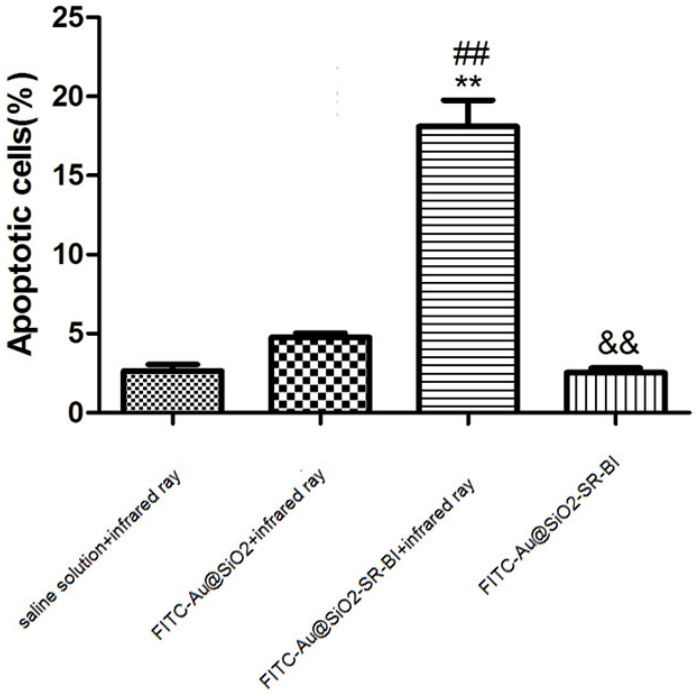

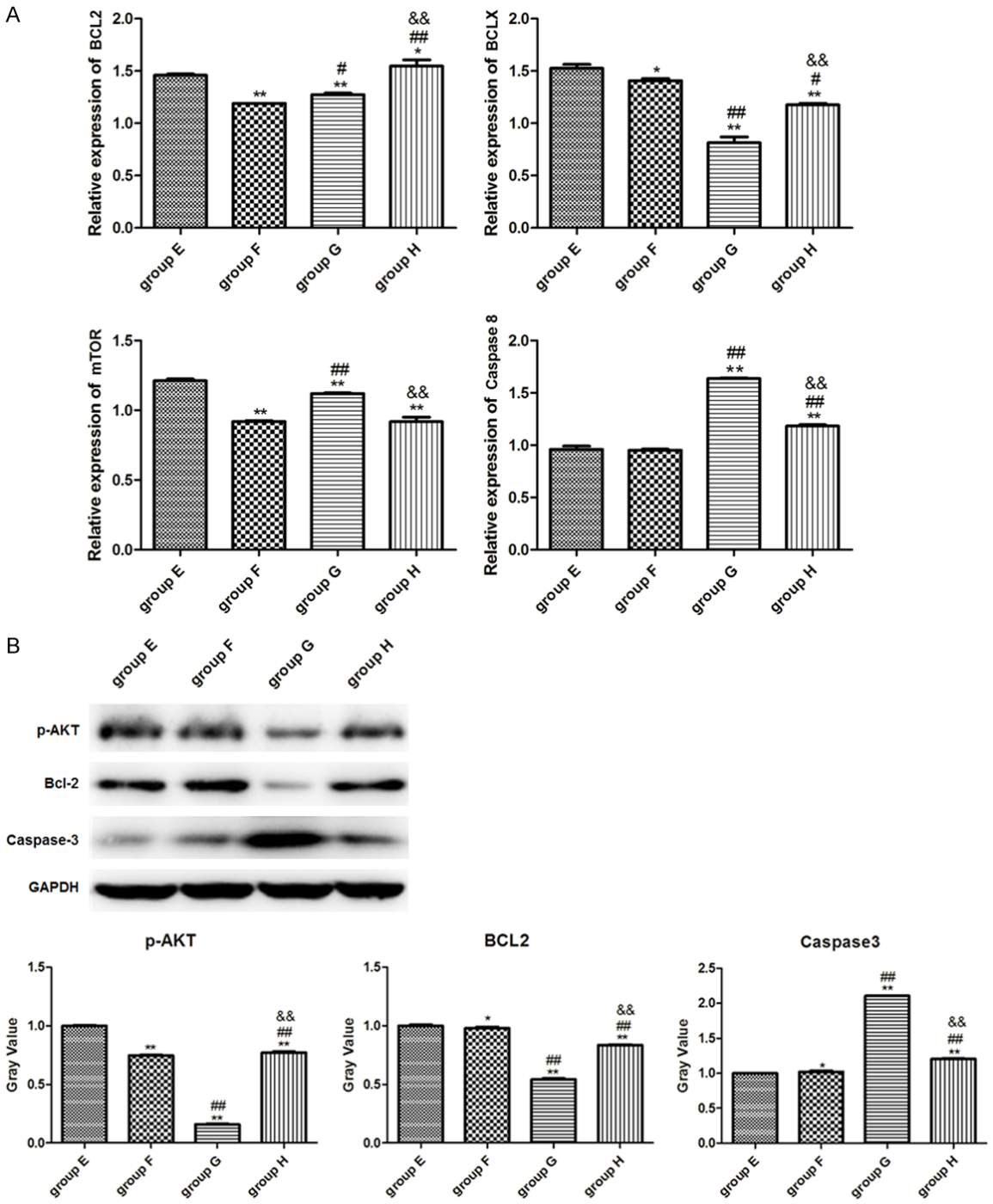

Figure 8. Quantitative polymerase chain reaction of tumor tissues after differential processing (groups E-H) (A). Western blotting of tumors tissues after differential processing (groups E-H) (B). $^{*}P<0.05$, $^{**}P<0.01$ compared with group E, $^{\#\#}P<0.01$ compared with group F, $^{\&\&}P<0.01$ compared with group G.

photothermal therapy of cervical cancer. To our best knowledge, very few studies have focused on testing Au@SiO_2-mediated targeted-therapy in cervical cancer.

The antibody-conjugated Au@SiO_2 synthesized in our study displayed good affinity for the cervical cancer cell line, MS751. Cellular uptake is a complicated process, which is influenced by several factors including particle size, composition, surface charge, and cell type [32, 33]. A previous study reported that antibody-conjugated gold nanospheres of 35 nm diameter act as efficient photothermal absorbers in

destroying cancer cells without affecting the surrounding normal cells [34]. Huang et al. [35] also demonstrated that the maximum uptake by cells occurred with particle size of 37 nm. The present study showed that the particle size of the nanoparticles ranged between 2-2.5 μm and the particles were negatively charged. However, the larger particle size and the negative charge did not affect their cellular affinity.

SR-BI is an 82-kDa glycoprotein receptor with two transmembrane domains, which plays a critical role in the metabolism of high-density lipoprotein [36]. Interestingly, lipid metabolism is a relevant target for cancer treatment [37]. Additionally, this integral membrane protein receptor is implicated in the metabolism of cholesterol by cancer cells, whereby overexpression of SR-BI has been observed in many tumors and cancer cell lines [38]. Overexpression of SR-BI can enhance high-density lipoproteins-mediated proliferation of the breast cancer cells via the PI3K/AP-1 pathway [39]. Thus, SR-BI has been considered as a potential marker for cancer diagnosis, prognosis, and treatment [40]. However, the role of SR-BI in cervical cancer has not been reported to our knowledge. In the present study, we coupled Au@SiO_2 with SR-BI for the targeted-therapy in cervical cancer. Moreover, we compared the expression level of SR-BI in H8 (normal cervical epithelial) and MS751 (cervical cancer) cells and found high expression of SR-BI in MS751 cells and low expression in H8 cells, suggesting that SR-BI was a specific protein in cervical epithelial cells.

Photothermal therapy utilizing nanoparticles was introduced for their effective destruction of cancer cells [23, 41]. A previous study has demonstrated the ability of antibody-coated nanoshells in targeting tumor cells in glioma and medulloblastoma [29]. In the present study, using TUNEL assay, we found significant apoptosis in FITC-Au@SiO_2-SR-BI group in both MS751 and H8 cells, while almost no apoptosis was found in groups without infrared irradiation or coupled antibodies. Our tumor formation experiments in nude mice showed that the tumor volume was significantly reduced in the FITC-Au@SiO_2-SR-BI group after infrared irradiation. HE staining revealed that numerous cells in the tumor tissue were contracted, while some cells were lysed and necrotic. The apoptotic rate of cells in FITC-Au@SiO_2-SR-BI group was also significantly increased, when compared to the other groups without infrared irradiation or coupled antibodies. Therefore, the apoptosis-related genes and proteins were analyzed in the tumor tissues. The results showed that BCL2, BCLX, mTOR, and p-AKT were significantly reduced in this group, while caspase 8 and caspase 3 were significantly increased. These results further suggested that SR-BI-conjugated FITC-Au@SiO_2 photothermal therapy is an effective method for targeting cervical cancer cells.

It has been reported that AuroLase therapy, a type of plasmonic photothermal therapy based on 150 nm silica-gold nanoshells that are coated with polyethylene glycol, absorb near-infrared light, and produce heat, has been under clinical trials (ClinicalTrials.gov Identifiers: NCT00848042 for refractory and/or recurrent tumors of the head and neck (2008-2014), NCT01679470 for metastatic lung tumors (2012-2014), and currently recruiting clinical NCT02680535 for localized prostate cancer (2016 until now)). The clinical trials for AuroLase are based on intravenous injections of silica-gold nanoshells in the blood. Due to leakage and poor organization of tumor blood vessels, these nanospheres can accumulate inside tumors via the enhanced permeability and retention effect [42]. In the present study, we preliminarily designed FITC-Au@SiO_2-SR-BI that can target cervical cancer cells via *in vitro* and *in vivo* experiments. Nevertheless, the toxicity, biodistribution, and pharmacokinetics of SR-BI-conjugated FITC-Au@SiO_2 photothermal therapy should be systematically studied. Thus, our future studies will focus on efficacy, mechanism, and toxicity in order to move this form of cancer therapy to the clinical stages.

There were some limitations in this study. The expression level of SR-B1 was not detected in the animal model. Additionally, the absorption and near-infrared laser hyperthermia efficiency were not measured. Therefore, further experiments are still needed to confirm the effect of this therapy in cervical cancer.

Conclusions

In conclusion, the study presented a novel antibody-conjugated Au@SiO_2 nanoparticle specifi-

cally targeting molecular receptors on cancer cell membranes. SR-BI-conjugated FITC-Au@SiO_2 photothermal therapy is an effective method for the targeting of cervical cancer cells. Antibody-conjugated Au@SiO_2 nanoparticles may have therapeutic potential in cervical cancer.

Acknowledgements

This work was supported by the Beijing Medical Award Foundation (No. YXJL-2020-0417-0043 and No. YXJL-2020-0510-0044), the Key Project of Petrel Foundation of Harbin Medical University Cancer Hospital (No. JJZD2020-07), the Cancer Prevention and Diagnosis and Treatment Scientific Research Foundation of Beijing Cancer Prevention and Treatment Society (No. 2020-1012).

Disclosure of conflict of interest

None.

Address correspondence to: Yaoxian Wang and Xiuwei Chen, Department of Gynecology, Harbin Medical University Cancer Hospital, No. 150 Haping Road, Nangang District, Harbin 150081, Heilongjiang, China. Tel: +86-0451-86298578; E-mail: wyxxs012@126.com (YXW); chenxiuwei1023@163.com (XWC)

References

[1] Ferlay J, Soerjomataram I, Dikshit R, Eser S, Mathers C, Rebelo M, Parkin DM, Forman D and Bray F. Cancer incidence and mortality worldwide: sources, methods and major patterns in GLOBOCAN 2012. Int J Cancer 2015; 136: E359-E386.

[2] Marth C, Landoni F, Mahner S, McCormack M, Gonzalez-Martin A and Colombo N; ESMO Guidelines Committee. Cervical cancer: ESMO clinical practice guidelines for diagnosis, treatment and follow-up. Ann Oncol 2017; 28: iv72-iv83.

[3] Uyar D and Rader J. Genomics of cervical cancer and the role of human papillomavirus pathobiology. Clin Chem 2014; 60: 144-146.

[4] Peng L, Yuan X, Jiang B, Tang Z and Li GC. LncRNAs: key players and novel insights into cervical cancer. Tumour Biol 2016; 37: 2779-2788.

[5] Rai P, Mallidi S, Zheng X, Rahmanzadeh R, Mir Y, Elrington S, Khurshid A and Hasan T. Development and applications of photo-triggered theranostic agents. Adv Drug Deliver Rev 2010; 62: 1094-1124.

[6] Xie J, Lee S and Chen X. Nanoparticle-based theranostic agents. Adv Drug Deliver Rev 2010; 62: 1064-1079.

[7] Xie J, Liu G, Eden HS, Ai H and Chen X. Surface-engineered magnetic nanoparticle platforms for cancer imaging and therapy. Acc Chem Res 2011; 44: 883-892.

[8] Xu X, Zhang K, Zhao L, Wang D, Bu W, Zheng C and Sun H. Characteristics of three sizes of silica nanoparticles in the osteoblastic cell line, MC3T3-E1. RSC Adv 2014; 4: 46481-46487.

[9] Lu D, Ouyang S, Xu H, Li D, Zhang X, Li Y and Ye J. Designing Au surface-modified nanoporous-single-crystalline SrTiO3 to optimize diffusion of surface plasmon resonance-induce photoelectron toward enhanced visible-light photoactivity. ACS Appl Mater Inter 2016; 8: 9506-9513.

[10] Jeong S, Song J, Lee W, Ryu YM, Jung Y, Kim SY, Kim K, Hong SC, Myung SJ and Kim S. Cancer-microenvironment-sensitive activatable quantum dot probe in the second near-infrared window. Nano Lett 2017; 17: 1378-1386.

[11] Kim DH and Larson AC. Deoxycholate bile acid directed synthesis of branched Au nanostructures for near infrared photothermal ablation. Biomaterials 2015; 56: 154-164.

[12] Chen J, Glaus C, Laforest R, Zhang Q, Yang M, Gidding M, Welch MJ and Xia Y. Gold nanocages as photothermal transducers for cancer treatment. Small 2010; 6: 811-817.

[13] Bardhan R, Chen W, Bartels M, Perez-Torres C, Botero MF, McAninch RW, Contreras A, Schiff R, Pautler RG, Halas NJ and Joshi A. Tracking of multimodal therapeutic nanocomplexes targeting breast cancer in vivo. Nano Lett 2010; 10: 4920-4928.

[14] Cobley CM, Chen J, Cho EC, Wang LV and Xia Y. Gold nanostructures: a class of multifunctional materials for biomedical applications. Chem Soc Rev 2011; 40: 44-56.

[15] Wang S, Liu K, Liu J, Yu ZT, Xu X, Zhao L, Lee T, Lee EK, Reiss J, Lee YK, Chung LW, Huang J, Rettig M, Seligson D, Duraiswamy KN, Shen CK and Tseng HR. Highly efficient capture of circulating tumor cells by using nanostructured silicon substrates with integrated chaotic micromixers. Angew Chem Int Edit 2011; 50: 3084-3088.

[16] Chen B, Xia Z, Deng YN, Yang Y, Zhang P, Zhu H, Xu N and Liang S. Emerging microRNA biomarkers for colorectal cancer diagnosis and prognosis. Open Biol 2019; 9: 180212.

[17] Li VA, Scialabba C, Vetri V, Cavallaro G, Licciardi M and Giammona G. Near-infrared light

responsive folate targeted gold nanorods for combined photothermal-chemotherapy of osteosarcoma. ACS Appl Mater Inter 2017; 9: 14453-14469.
[18] Li J, Xu L, Wang H, Yang B, Liu H, Pan W and Li S. Comparison of bare and amino modified mesoporous silica@ poly (ethyleneimine) s xerogel as indomethacin carrier: superiority of amino modification. Mater Sci Eng C Mater Biol Appl 2016; 59: 710-716.
[19] Liu S and Han M. Synthesis, functionalization, and bioconjugation of monodisperse, Silica-Coated gold nanoparticles: robust bioprobes. Adv Funct Mater 2005; 15: 961-967.
[20] Mallick S, Sun IC, Kim K and Yi DK. Silica coated gold nanorods for imaging and photo-thermal therapy of cancer cells. J Nanosci Nanotechno 2013; 13: 3223-3229.
[21] Zhang Z, Wang L, Wang J, Jiang X, Li X, Hu Z, Ji Y, Wu X and Chen C. Mesoporous silica-coated gold nanorods as a light-mediated multifunctional theranostic platform for cancer treatment. Adv Mater 2012; 24: 1418-1423.
[22] Yavuz MS, Cheng Y, Chen J, Cobley CM, Zhang Q, Rycenga M, Xie J, Kim C, Song KH, Schwartz AG, Wang LV and Xia Y. Gold nanocages covered by smart polymers for controlled release with near-infrared light. Nat Mater 2009; 8: 935-939.
[23] Ayala-Orozco C, Urban C, Knight MW, Urban AS, Neumann O, Bishnoi SW, Mukherjee S, Goodman AM, Charron H, Mitchell T, Shea M, Roy R, Nanda S, Schiff R, Halas NJ and Joshi A. Au nanomatryoshkas as efficient near-infrared photothermal transducers for cancer treatment: benchmarking against nanoshells. ACS Nano 2014; 8: 6372-6381.
[24] Hu X, Schwarz JK, Lewis JS, Huettner PC, Rader JS, Deasy JO, Grigsby PW and Wang X. A microRNA expression signature for cervical cancer prognosis. Cancer Res 2010; 70: 1441-1448.
[25] Gournaris E, Park W, Cho S, Bentrem DJ, Larson AC and Kim DH. Near-infrared fluorescent endoscopic image-guided photothermal ablation therapy of colorectal cancer using dual-modal gold nanorods targeting tumor infiltrating innate immune cells in transgenic TS4 CRE/APCloxΔ468 mouse model. ACS Appl Mater Inter 2019; 11: 21353-21359.
[26] Liu Y, Chongsathidkiet P, Crawford BM, Odion R, Dechant CA, Kemeny HR, Cui X, Maccarini PF, Lascola CD and Fecci PE. Plasmonic gold nanostar-mediated photothermal immunotherapy for brain tumor ablation and immunologic memory. Immunotherapy 2019; 11: 1293-1302.
[27] Poursalehi Z, Salehi R, Samadi N, Rasta SH, Mansoori B and Majdi H. A simple strategy for chemo-photothermal ablation of breast cancer cells by novel smart gold nanoparticles. Photodiagnosis Photodyn Ther 2019; 28: 25-37.
[28] Gobin AM, Lee MH, Halas NJ, James WD, Drezek RA and West JL. Near-infrared resonant nanoshells for combined optical imaging and photothermal cancer therapy. Nano lett 2007; 7: 1929-1934.
[29] Bernardi RJ, Lowery AR, Thompson PA, Blaney SM and West JL. Immunonanoshells for targeted photothermal ablation in medulloblastoma and glioma: an in vitro evaluation using human cell lines. J Neurooncol 2008; 86: 165-172.
[30] Day ES, Thompson PA, Zhang L, Lewinski NA, Ahmed N, Drezek RA, Blaney SM and West JL. Nanoshell-mediated photothermal therapy improves survival in a murine glioma model. J Neurooncol 2011; 104: 55-63.
[31] Lowery AR, Gobin AM, Day ES, Halas NJ and West JL. Immunonanoshells for targeted photothermal ablation of tumor cells. Int J Nanomed 2006; 1: 149-54.
[32] Zhao ZJ, Xu GL and L Z. Study on clinical and serum levels chandes of monoamine nurrotransmitters in children with attention deficit hyperactivity disorder. J Clin Psychiat 2010; 20: 293-296.
[33] Chithrani BD and Chan WC. Elucidating the mechanism of cellular uptake and removal of protein-coated gold nanoparticles of different sizes and shapes. Nano Lett 2007; 7: 1542-1550.
[34] El-Sayed IH, Huang X and El-Sayed MA. Surface plasmon resonance scattering and absorption of anti-EGFR antibody conjugated gold nanoparticles in cancer diagnostics: applications in oral cancer. Nano Lett 2005; 5: 829-834.
[35] Huang J, Bu L, Xie J, Chen K, Cheng Z, Li X and Chen X. Effects of nanoparticle size on cellular uptake and liver MRI with polyvinylpyrrolidone-coated iron oxide nanoparticles. ACS Nano 2010; 4: 7151-7160.
[36] Krieger M. Charting the fate of the "good cholesterol": identification and characterization of the high-density lipoprotein receptor SR-BI. Annu Rev Biochem 1999; 68: 523-558.
[37] Gutierrez-Pajares JL, Ben Hassen C, Chevalier S and Frank PG. SR-BI: linking cholesterol and lipoprotein metabolism with breast and prostate cancer. Front Pharmacol 2016; 7: 338.
[38] Rajora MA and Zheng G. Targeting SR-BI for cancer diagnostics, imaging and therapy. Front Pharmacol 2016; 7: 326.
[39] Cao WM, Murao K, Imachi H, Yu X, Abe H, Yamauchi A, Niimi M, Miyauchi A, Wong NC and Ishida T. A mutant high-density lipoprotein receptor inhibits proliferation of human breast

cancer cells. Cancer Res 2004; 64: 1515-1521.
[40] Wang D, Huang J, Gui T, Yang Y, Feng T, Tzvetkov NT, Xu T, Gai Z, Zhou Y and Zhang J. SR-BI as a target of natural products and its significance in cancer. Semin Cancer Biol 2020; [Epub ahead of print].
[41] Huang X, El-Sayed IH, Qian W and El-Sayed MA. Cancer cell imaging and photothermal therapy in the near-infrared region by using gold nanorods. J Am Chem Soc 2006; 128: 2115-2120.
[42] Ali MR, Wu Y and El-Sayed MA. Gold-nanoparticle-assisted plasmonic photothermal therapy advances toward clinical application. J Phys Chem C 2019; 123: 15375-15393.

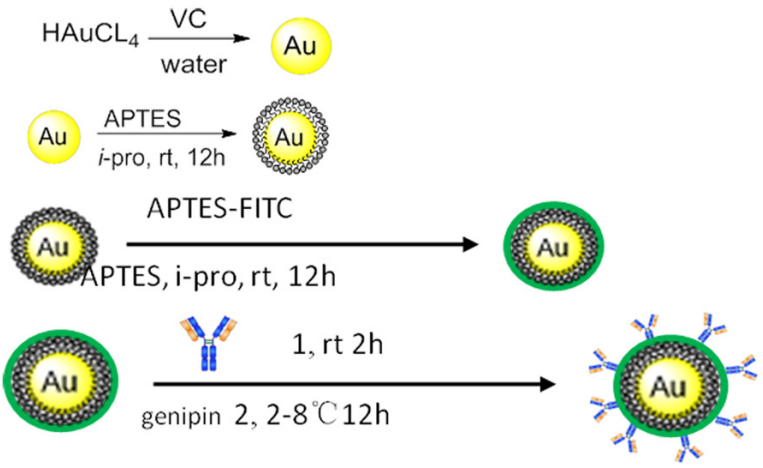

Figure S1. The schematic illustration of the preparation of FITC-Au@SiO2-SR-BI antibody.